Multi-Layered Circular Dielectric Structure SAR Imaging Using Time reversal-Compressed Sensing Algorithms Based on Non-uniform Measurement

Baolong Wu, Guillermo Álvarez-Narciandi, Jaime Laviada

***Abstract*—In this letter, an algorithm for synthetic aperture radar (SAR) imaging of electrically small targets embedded in multilayered cylindrical geometries (e.g., pipes) using non-uniform measurement points is presented. In contrast to previous approaches, this algorithm is able to efficiently handle non-uniform points without exhibiting relevant side lobes in the image. For these purposes, the approach exploits a flexible time-reversal (TR) algorithm enhanced by compressed sensing (CS). The theoretical performance of the algorithm is studied in terms of the point spread function (PSF) and several images are presented using synthetic full-wave data from CST Microwave Studio®. In addition, the approach is empirically validated by performing microwave imaging of a PVC pipe. The results demonstrated that the TR-CS algorithm provides an effective focusing technique for dense non-uniform measurement points, as well as for sparse non-uniform measurement points.**

***Index Terms*—Synthetic aperture radar (SAR) imaging, multilayer cylindrical geometries, microwave imaging, circular SAR, compressed sensing.**

I. Introduction

In the context of airborne synthetic aperture radar (SAR) imaging systems, circular scanning (i.e., circular synthetic aperture) enables the acquisition of information from an object or a scene from multiple views (angles), resulting in the approach known as circular-SAR (C-SAR) [1–7]. Despite this imaging technique is very appealing for cylindrically layered dielectric structures (e.g., pipes), some interesting nondestructive testing (NDT) applications, such as the detection of flaws or foreign objects embedded in the geometry, cannot be directly solved by this technique as C-SAR usually assumes free-space propagation.

Several SAR imaging techniques based on Green's functions [8-10] have been proposed to take into account the multilayered planar geometry, whose radii of layers and dielectric properties are known in general. Later, some of these formulations have been adapted to multilayered cylindrical media. In particular, several approaches based on Green's function (GF) deconvolution and time-reversal (TR) have been proposed. The different approaches provide several advantages in terms of three parameters: i) image side lobe level (SLL), ii) capacity of dealing with non-uniform data and iii) multiple reflections capabilities.

Approaches based on GF are able to take into account the effect of multiple reflections at the expense of a complex formulation [11]. Moreover, GF approaches must be modified to use non-uniform data as proposed in [12].

In contrast, TR approaches usually neglect these multiple reflections, but they provide a very flexible formulation to be able to deal with non-uniform acquisitions [13].

A drawback of both GF and TR approaches is that they exhibit a relatively high SLL (8-10 dB). However, it has been shown that TR using uniform data can benefit from compressed sensing (CS) to drastically decrease this level in the case of sparse targets [14], which is very common in NDT applications.

Non-uniform data is becoming quite relevant due to recent developments in electromagnetic imaging using portable scanners, which are handled by hand so they avoid the use of bulky mechanical positioners [15-17] at the expense of acquiring data at non-uniform positions.

In this letter, the TR-CS approach for imaging of cylindrically layered geometries presented in [14] is modified to efficiently deal with non-uniform data whereas it preserves low SLL imaging capabilities.

II. Non-uniform Multi-layered TR-CS Method

In Fig. 1(a), similar to [12], the schematic of the non-uniform measurement case for three-layered circular dielectric structures is depicted. The first layer corresponds to the background medium, which is typically air. The non-uniform discrete measurement points, which were located in the first layer, are represented by "▲". The second and third layers are the imaging domain. They were made up of two different materials (i.e., different dielectric constants). The targets to be imaged, are

B. Wu is with the College of Computer Science and Electronic Engineering, Hunan University, China. (e-mail: wubaolongyou@163.com). G. Álvarez-Narciandi and J. Laviada are with the Department of Electrical Engineering, University of Oviedo, Gijón, 33203, Spain (e-mail: laviadajaime@uniovi.es).

located in the inner layer and represented by "●".

In a similar fashion to the TR algorithm [13], the first step of the TR-CS imaging algorithm is to find the transmission/refraction path of the electromagnetic wave between each non-uniform measurement point and the imaging pixel. Fig. 1(b) depicts the transmission/refraction path of three-layered circular dielectric object for one fixed measurement point. In Fig. 1(b), S_1 denotes the measurement point, P_{image} denotes the pixel to be imaged in the third layer and S_2 and S_3 denote the intersection points of the path of the electromagnetic wave traveling from S_1 with layers 2 and 3, respectively. O is the center of the multi-layered circular dielectric object.

Once the path optimization method proposed in [13] is applied to find the transmission/refraction path, it is possible to estimate a reference signal, which models the response of an ideal point target at the imaging pixel, by

$$S_{ref}\left(x_i,y_j,x_l^{'},y_l^{'}\right)=\left[\tau_{12(round-trip)}\tau_{23(round-trip)}\exp\left(-j2\left(k_1\left|\overrightarrow{S_1S_2}\right|+k_2\left|\overrightarrow{S_2S_3}\right|+k_3\left|\overrightarrow{S_3P_{image}}\right|\right)\right)\right]_{\left(x_i,y_j,x_l^{'},y_l^{'}\right)}, \quad (1)$$

where " $\left|\overrightarrow{\ }\right|$ " denotes the vector norm. k_m denotes the wavenumber of the mth layer. τ_{mn} denotes the transmission coefficient at the boundary between the mth and n th layers. $S_{ref}\left(x_i,y_j,x_l^{'},y_l^{'}\right)$ is the reference signal with respect to the variables x_i , y_j, and $x_l^{'}$, $y_l^{'}$. $\left(x_i,y_j\right)$ denotes the position to be imaged in line *i* and column *j* (i.e., P_{image} in Fig. 1(b)), and $\left(x_l^{'},y_l^{'}\right)$ denotes the position of the *l*th measurement point.

At this stage, it is possible to formulate a TR algorithm compatible with non-uniform sampling by resorting to the standard TR imaging formulation [13]:

$$f\left(x_i,y_j\right)=\sum_{x_l^{'},y_l}S_{1(rec)}\left(x_l^{'},y_l^{'}\right)S_{ref}^{*}\left(x_i,y_j,x_l^{'},y_l^{'}\right) \quad (2)$$

where $f\left(x_i,y_j\right)$ is the value at position $\left(x_i,y_j\right)$, $S_{1(rec)}\left(x_l^{'},y_l^{'}\right)$ is the received signal measured at the position $\left(x_l^{'},y_l^{'}\right)$. The superscript * denotes conjugate.

Let us define some elements from (2) in terms of matrices and vectors as in [14]:

$$R=\begin{bmatrix} S_{ref}\left(x_1,y_1,x_1^{'},y_1^{'}\right) & S_{ref}\left(x_1,y_2,x_1^{'},y_1^{'}\right) & \cdots & S_{ref}\left(x_M,y_N,x_1^{'},y_1^{'}\right) \\ S_{ref}\left(x_1,y_1,x_2^{'},y_2^{'}\right) & S_{ref}\left(x_1,y_2,x_2^{'},y_2^{'}\right) & \cdots & S_{ref}\left(x_M,y_N,x_2^{'},y_2^{'}\right) \\ \cdots & \cdots & \cdots & \cdots \\ S_{ref}\left(x_1,y_1,x_L^{'},y_L^{'}\right) & S_{ref}\left(x_1,y_2,x_L^{'},y_L^{'}\right) & \cdots & S_{ref}\left(x_M,y_N,x_L^{'},y_L^{'}\right) \end{bmatrix} \quad (3)$$

$$\mathrm{g}=\left[S_{1(rec)}\left(x_1^{'},y_1^{'}\right) \quad S_{1(rec)}\left(x_2^{'},y_2^{'}\right) \quad \cdots \quad S_{1(rec)}\left(x_L^{'},y_L^{'}\right)\right]^T \quad (4)$$

$$\gamma=\left[f\left(x_1,y_1\right) \quad f\left(x_1,y_2\right) \quad \cdots \quad f\left(x_M,y_N\right)\right]^T, \quad (5)$$

where R is the mapping matrix with $M\times N$ columns and L rows, M and N represent the line and column number of the pixels of the imaging area, respectively. L represents the number of non-uniform measurement points. g is the measurement matrix,

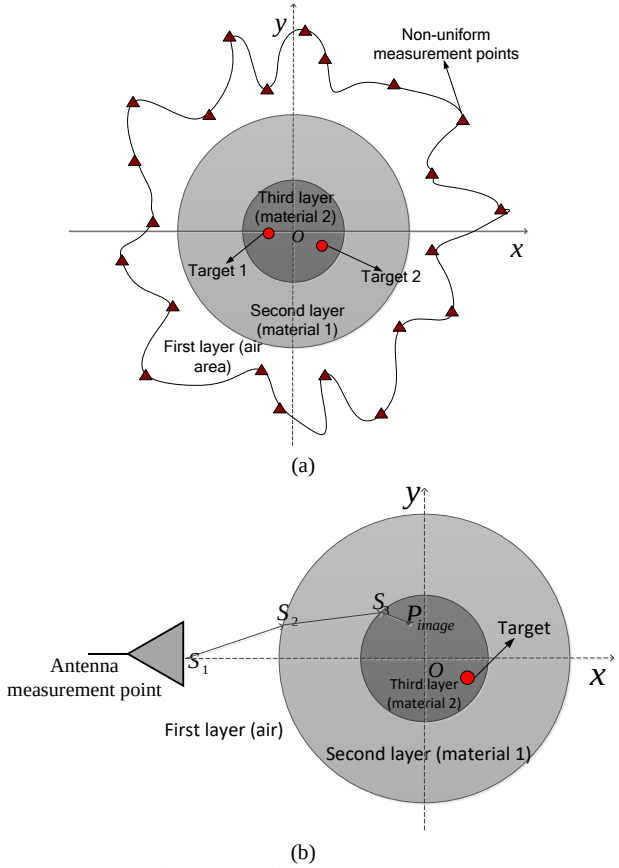

Fig.1. (a) Schematic of the non-uniform measurement points acquired around the three-layered circular dielectric object; (b) Schematic of transmission/refraction path of three-layered circular dielectric object for one fixed measurement point.

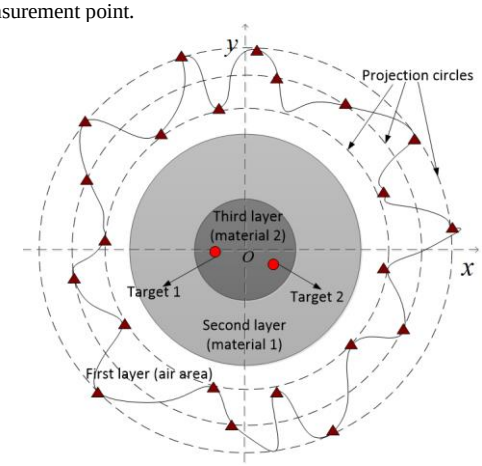

Fig.2. Schematic of the projection circles for non-uniform measurement points.

which includes the received signals of all of the measurement points. γ is the coefficient matrix with the $M\times N$ pixel values.

Taking into account the previous definitions, the image inside the multi-layered circular dielectric object can be expressed in terms of a non-uniform CS problem by means of

$$\gamma=\arg\min_{\gamma}\left(\left\|g-R\gamma\right\|_2^2+\lambda\left\|\gamma\right\|_1\right), \quad (6)$$

where the scalar λ controls the balance between the fitting error and the sparse degree. In practical applications, λ can be chosen by a prior trial using a standard sample pipe. Then, this trained λ value could be used as an empirical parameter for

other similar imaging scenarios. $\| \|_1$ and $\| \|_2$ denote the 1-norm and 2-norm, respectively. The image reconstruction approach based on (6) is specifically proposed for high-resolution detection of point-like small targets due to the sparse nature of the solution to CS problems. For distributed targets, an additional term accounting for the total variation (TV) norm can be added to (6) to obtain a better performance [18].

The TR-CS imaging algorithm for non-uniform acquisitions given by (6) involves evaluating the reference signal for every combination of measurement point and image pixel. Consequently, if L denotes the number of non-uniform acquisition points, N_r and N_a denote number of pixels along the radial and angular directions, then the computational complexity of reference signal computing is $L \times N_r \times N_a$.

If the number of the measurement points were very large, the computation time would also be very long. In order to improve the computational efficiency, the acquisition points can be projected into a regular grid of virtual points located on projection circles [12] so that these virtual points are equally spaced along the angular and radial directions (see Fig. 2). For this purpose, the measurement points are projected to the nearest virtual point while the remaining virtual points are set to zero. After that, the TR-CS algorithm given by (1)-(6) is applied to the virtual points instead of the real measurement points. The main advantage is that the virtual points are equally-spaced along the angular direction and, therefore, the reference signals in (1) can be fast calculated by applying rotation symmetry since any rotation of the transmitter position will result in the same reference signals. Consequently, only one reference path is required per projection circle as the rest of reference paths are found by rotation.

If the number of the projection circles is denoted by N_c, then the computational complexity would be $N_c \times N_r \times N_a$. In general, for a dense measurement, the number of non-uniform measurement points is much greater than the number of the projection circles, i.e. $L >> N_c$ significantly reducing the computational time.

It should be noted that the TR formulation does not take into account multiple reflections between different layers. If the dielectric contrast between layers is not large, then the multiple reflections will be negligible as shown in [13]. Nevertheless, scenarios exhibiting high contrast and, therefore, stronger reflections should be managed by other formulations such as the ones based on GFs at the expense of losing the CS advantages in terms of low SLL.

III. Simulation Results

In order to explore the performance of the TR-CS algorithm, the point spread function (PSF) was firstly analyzed. The echoed signal of an ideal point target was simulated in Matlab using (1) to calculate the received signal for a point target at a given location. In addition, the PSF of the TR algorithm given by (2) is used as a reference result. This analysis was done for a geometry with outer surface at 62.8 mm and inner surface at 59.3 mm (see Fig. 1). A total of 314 acquisition points was used.

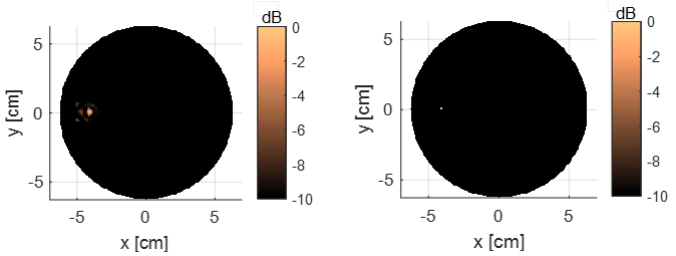

Fig. 3 Ideal point spread function (PSF) of 314 non-uniform measurement points in the Matlab simulation example. (a) TR algorithm-based (b) TR-CS algorithm-based.

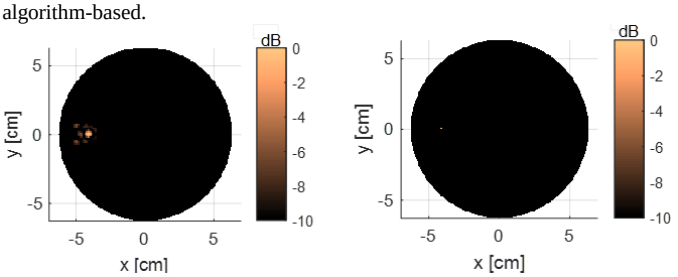

Fig. 4 Imaging result for the TR and TR-CS algorithms when random errors were introduced for the cases in Fig.3. (a) For Fig. 3(a); (b) For Fig. 3(b);

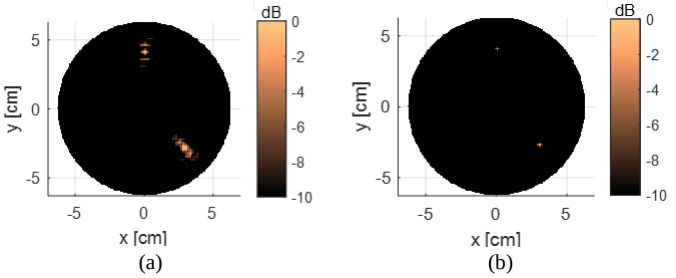

Fig. 5 Imaging result of two targets using 70 non-uniform measurement points. (a) TR algorithm-based; (b) TR-CS algorithm-based.

These points were randomly placed at a radial distance in the range of 90 mm and 110 mm from the center. The optimized pre-processing by means of projection circles described in Section II was used with radial and angular steps of 1 mm and 1º, respectively. The projection circles ranged from 90mm to 110mm. In order to match the parameter settings of the real experiment shown later, in this simulation, the relative dielectric constant of the first, second, and third layer of the simulated three-layered C-SAR imaging structure was also set to ε_r=1, ε_r =2.2, and ε_r=2.4, respectively. The ideal point target was set at a position with a radius of 41.4 mm. Finally, the frequency response was sampled at 51 equally-spaced frequencies ranging from 8.3 GHz to 12.3 GHz.

As shown in Fig. 3, the PSF of the multi-layered circular dielectric structure based on the TR algorithm for non-uniform samples and the proposed TR-CS algorithm are well focused. However, TR-CS algorithm clearly outperforms the TR algorithm providing super resolution for this ideal point target.

In order to investigate the robustness of the presented imaging algorithm with respect to projection errors and location measurement errors of the acquisition points, random location errors (a uniform distribution between ±5mm) were added in the simulated echoed signal. The corresponding imaging results are shown in Fig. 4 revealing that the algorithm is stable for

moderate positioning errors showing that the algorithm is suitable for practical applications.

In order to assess the presented imaging algorithm further, CST Microwave Studio® was used to generate the simulated echoed signal of multi-layered circular dielectric structures with small targets. In the CST simulation, the parameters setup of the imaging scenario, including frequency range, radii and relative dielectric constants of the multi-layered circular structure, were set to the same as the Matlab simulation discussed above and the real experiment shown later. In the CST model, two small metallic cylinders with a radius of 2 mm and a length of 20 mm were embedded inside the inner layer. The radius of both targets was 40.2 mm from the center of the cylinder and the relative angular separation between them was 135 degrees.

The corresponding imaging results are shown in Fig. 5. It shows that the algorithm is also able to correctly detect both targets. It is worth noting that the estimated reflectivity is higher for one of the two identical targets. Although it happens for both algorithms (TR and TR-CS) due to asymmetries in the non-uniform sampling, it is more significant for the TR-CS algorithm due to the tendency of CS algorithms to focus the energy in small areas. However, this CS feature also results in a much better resolution with negligible artifacts.

IV. Real Experimental Results

In order to verify the effectiveness of the presented algorithm with measurement data, the setup shown in Fig. 6(a) was used. In this setup, an open-ended rectangular waveguide (OEWG) was used to transmit and receive a continuous-wave stepped-frequency electromagnetic signal. The signal was generated by means of a vector network analyzer, which acquired the S11 parameter of 201 equally-spaced frequency points between 8.3 and 12.3 GHz. The OEWG was mounted on a robot-arm with the capability to move along the three-orthogonal axes (defined as xyz axes). The PVC pipe was put on a turntable, which could be turned to any arbitrary measurement angle. Thus, the system enabled to simulate arbitrary acquisition angles and radii.

In this experiment, two screws were put at the same height inside a PVC pipe full of sand. The head diameter, body diameter, and height of the screws were 9.85 mm, 5.86 mm, and 22.16 mm, respectively. The inner radius and the thickness of the pipe were 59.3 mm and 3.5 mm, respectively. This circular geometry together with the screws, before being completely covered with sand, is shown in Fig. 6(b). The relative dielectric constants of the PVC pipe and sand used in the experiment at this frequency band were 2.2 and 2.4, respectively. The S11 parameter was acquired at 1000 (dense case) measurement points using a random angular step, respectively. The radii of the sampling measurement points were also randomly generated at a range from 90 mm to 110 mm. Regarding the projection circles to speed-up the path calculation, the same setup as for the PSF calculation was used.

Figs. 7-8 show the corresponding imaging results. From these microwave images, we can see that the TR-CS algorithm has a robust focusing performance even if only 63 (randomly picked) points are used to model a sparse measurement. In addition to the enhanced resolution, the TR-CS algorithm does not exhibit relevant image side lobes, which are always visible not only in the TR algorithm, but even in the case of using uniform sampling and enhanced propagation models such as in the case of algorithms based on Green's functions [11].

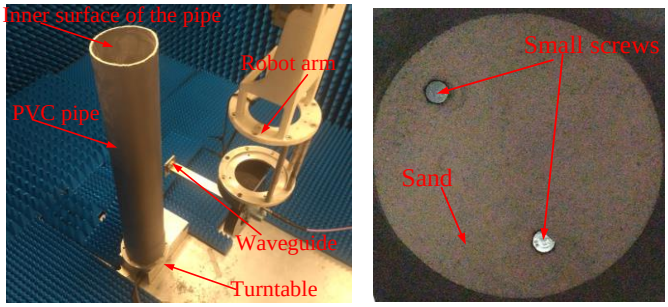

(a) (b)

Fig. 6 (a) Measurement setup; (b) Top view inside the polyvinyl chloride (PVC) pipe with the two screws before being completely covered by sand.

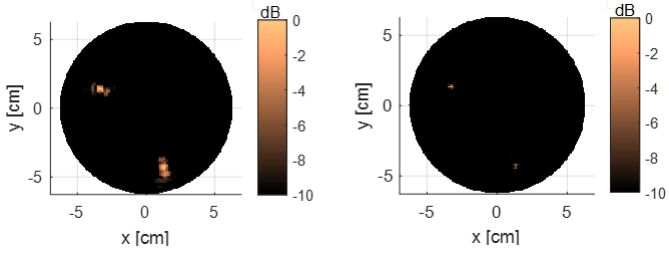

(a) (b)

Fig. 7 Imaging result of 1000 non-uniform measurement points (i.e., dense measurement) in the real experiment when the scan radius ranged from 90 mm to 110 mm randomly. (a) TR algorithm-based; (b) TR-CS algorithm-based.

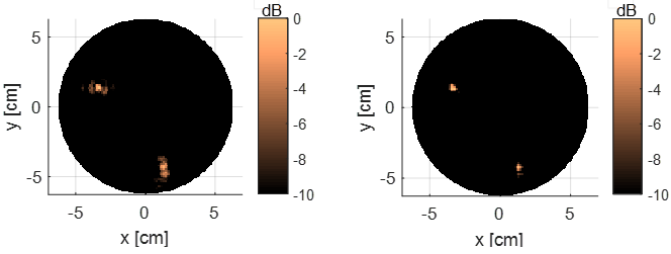

(a) (b)

Fig. 8 Imaging result of 63 non-uniform measurement points (i.e., sparse measurement) in the real experiment when the scan radius ranged from 90 mm to 110 mm randomly. (a) TR algorithm-based; (b) TR-CS algorithm-based.

V. Conclusion

In this letter, a TR-CS algorithm for the SAR imaging of electrically small objects embedded into multi-layered circular dielectric objects based on non-uniform data was presented. In contrast to other algorithms such as the ones based on TR or Green's function deconvolution, the presented algorithm clearly outperforms the TR algorithms in terms of resolution and image side lobes as demonstrated by means of simulated and experimental data. Moreover, the approach is also stable against typical positioning errors such as the ones associated to typical tracking for non-uniform measurements as well as against sparse measurements. The main drawback of the method is that it tends to focus more energy on some targets due to the CS nature. Future research will focus on investigating the impact of the TV norm to mitigate this effect as well as to deal with distributed targets.

REFERENCES

[1] M. Soumekh,"Synthetic aperture radar signal processing," *New York: Wiley*, 1999.

[2] M. Soumekh, "Reconnaissance with slant plane circular SAR imaging," *IEEE Trans. Image Process.*, vol. 5, no. 8, pp. 1252-1265, Aug. 1996.

[3] K. E. Dungan, and L. C. Potter, "3-D imaging of vehicles using wide aperture radar," *IEEE Trans. Aerosp. Electron. Syst.*, vol. 47, no. 1, pp. 187-200, Jan. 2011.

[4] Z. Zhang, H. Lei, and Z. Lv, "Vehicle Layover Removal in Circular SAR Images via ROSL," *IEEE Geosci. Remote Sens. Lett.*, vol. 12, no. 12, pp. 2413-2417, Dec. 2015.

[5] M. L. Bryant, L. L. Gostin, and M. Soumekh, "3-D E-CSAR imaging of a T-72 tank and synthesis of its SAR reconstructions," *IEEE Trans. Aerosp. Electron. Syst.*, vol. 39, no. 1, pp. 211-227, Jan. 2003.

[6] O. Ponce, et al, "Fully polarimetric high-resolution 3-D imaging with circular SAR at L-band," *IEEE Trans. on Geosci. Remote Sens.*, vol. 52, no. 6, pp. 3074-3090, Jun. 2014.

[7] G. Jia, et al, "Fourier-based 2-D imaging algorithm for circular synthetic aperture radar: Analysis and application," *IEEE J. Sel. Topics Appl. Earth Observ.*, vol. 9, no. 1, pp. 475-489, Oct. 2016.

[8] M. Fallahpour, et al, "Piecewise and Wiener filter-based SAR techniques for monostatic microwave imaging of layered structures," *IEEE Trans. Antennas Propag.*, vol. 62, no. 1, pp. 282-294, Jan. 2014.

[9] M. Fallahpour, and R. Zoughi, "Fast 3-D qualitative method for through-wall imaging and structural health monitoring," *IEEE Geosci. Remote Sens. Lett.*, vol. 12, no. 12, pp. 2463-2467, Dec. 2015.

[10] H. Jung, and K. Kim, "Autofocusing Technique Based on Generalized Multilayer Stolt Migration," *IEEE Trans. on Geosci. Remote Sens.*, Nov. 2017.

[11] J. Laviada, B. Wu, M.T. Ghasr, and R. Zoughi, "Nondestructive Evaluation of Microwave-Penetrable Pipes by Synthetic Aperture Imaging Enhanced by Full-Wave Field Propagation Model", *IEEE Trans. on Instrum. and Meas.*, vol. 68, no. 4, pp. 1112-1119, Apr. 2019.

[12] B. Wu, G. Álvarez-Narciandi, and J. Laviada, "Multi-layered circular dielectric structures synthetic aperture radar imaging based on Green's function using non-uniform measurements," *Remote Sensing*, vol. 12, no. 7, Apr. 2020.

[13] B. Wu, Y. Gao., J. Laviada, M.T. Ghasr and R. Zoughi, "Time-Reversal SAR Imaging for Nondestructive Testing of Circular and Cylindrical Multi-Layered Dielectric Structures", *IEEE Trans. on Instrum. and Meas.*, vol. 69, no. 5, pp. 2057-2066, May. 2020.

[14] B. Wu, and L. He, "Multi-layered circular dielectric structure SAR imaging based on compressed sensing for FOD detection in NDT,"*IEEE Trans. on Instrum. and Meas.*, [(DOI 10.1109/TIM.2020.2980801, Early Access publication date: 16 March 2020, (print issue publication pending)].

[15] H. He, P. Maheshwari, and D. J. Pommerenke, "The development of an EM-field probing system for manual near-field scanning," *IEEE Trans. on Electromagn. Compat*, vol. 58, no. 2, pp. 356–363, April 2016.

[16] J. Laviada, M.T. Ghasr, M. Lopez-Portugues, F. Las-Heras and Reza Zoughi, "Real-Time Multiview SAR Imaging Using a Portable Microwave Camera With Arbitrary Movement," *IEEE Trans. Antennas Propag.*, vol. 66, no. 12, pp. 7305-7314, Dec. 2018.

[17] G. Álvarez-Narciandi, M. López-Portugués, F. Las-Heras and J. Laviada, "Freehand, Agile, and High-Resolution Imaging With Compact mm-Wave Radar," *IEEE Access*, vol. 7, pp. 95516-95526, 2019.

[18] D. Bi, et al, "Multifrequency compressed sensing for 2-D near-field synthetic aperture radar image reconstruction", *IEEE Trans. on Instrum. and Meas.*, vol. 66, no. 4, pp. 777-791, Apr. 2017.